

## NASA's Hurricane and Severe Storm Sentinel (HS3) Investigation

Scott A. Braun, Paul A. Newman, Gerald M. Heymsfield

NASA Goddard Space Flight Center, Greenbelt, Maryland

Submitted to Bulletin of the American Meteor. Society

October 14, 2015

Corresponding author: Scott A. Braun, NASA Goddard Space Flight Center, Code 612,  
Greenbelt, MD 20771

Email: [scott.a.braun@nasa.gov](mailto:scott.a.braun@nasa.gov)

15

## Abstract

16 The National Aeronautics and Space Administrations's (NASA) Hurricane and Severe Storm  
17 Sentinel (HS3) investigation was a multi-year field campaign designed to improve understanding  
18 of the physical processes that control hurricane formation and intensity change, specifically the  
19 relative roles of environmental and inner-core processes. Funded as part of NASA's Earth  
20 Venture program, HS3 conducted five-week campaigns during the hurricane seasons of 2012-14  
21 using the NASA Global Hawk aircraft, along with a second Global Hawk in 2013 and a WB-57f  
22 aircraft in 2014. Flying from a base at Wallops Island, Virginia, the Global Hawk could be on  
23 station over storms for up to 18 hours off the East Coast of the U.S. to about 6 hours off the  
24 western coast of Africa. Over the three years, HS3 flew 21 missions over 9 named storms, along  
25 with flights over two non-developing systems and several Saharan Air Layer (SAL) outbreaks.  
26 This article summarizes the HS3 experiment, the missions flown, and some preliminary findings  
27 related to the rapid intensification and outflow structure of Hurricane Edouard (2014) and the  
28 interaction of Hurricane Nadine (2012) with the SAL.

29

A multi-year field campaign to measure environmental and inner-core processes that lead to storm formation and intensification into major hurricanes.

30

31       Almost 60 million Americans live within counties along the East and Gulf Coasts (140  
32 million total in East and Gulf coast states), thus exposing them to the potential destruction  
33 caused by a landfalling hurricane. Societal vulnerability to damage has increased primarily  
34 because of growth in both population and wealth in coastal zones from Texas to Maine. Pielke et  
35 al. (2008) projected a doubling of economic losses from landfalling hurricanes every ten years.  
36 Advances in airborne and satellite observing systems, computing technologies, numerical models,  
37 and scientific understanding of hurricanes have led to significant advances in the understanding  
38 of hurricane motion and subsequent improvements in track prediction. However, improvements  
39 in prediction of storm intensity change have lagged due to an inadequate understanding of  
40 the processes that cause it, insufficient sampling of appropriate observations of the storm  
41 environment and internal processes, and inadequate representation of those processes in  
42 models (Rogers et al. 2006).

43       For five weeks in each of the hurricane seasons of 2012-2014, the National Aeronautics and  
44 Space Administration (NASA) conducted airborne campaigns using high-altitude long-duration  
45 Unmanned Airborne Systems (UASs) to investigate the processes that underlie hurricane  
46 formation and intensification. The Hurricane and Severe Storm Sentinel (HS3) mission, funded  
47 under NASA's Earth Venture program, comprised a set of aircraft and payloads well suited for  
48 the study of hurricanes and other severe weather systems. Using data from two Global Hawk  
49 (GH) UASs, the HS3 goal was to better understand the physical processes that control intensity

change, specifically the relative roles of environmental and inner-core processes. This goal was focused on the following science questions:

Environment:

1. What impact does the Saharan Air Layer (SAL) have on intensity change?
2. How do storms interact with shear produced by large-scale wind systems?
3. How does the outflow layer interact with the environment?

Inner core:

1. What is the role of deep convective towers (bursts) in intensity change? Are they critical to intensification?
2. What changes in storm structure occur prior to and during genesis and rapid intensification?
3. How do intrusions of dry air impact intensity change?

HS3 was designed to address these questions and to assess the impact, both in terms of research and applications, of remote and in-situ data sets from the Global Hawks on modeling and analysis. During its three deployments (Aug.-Sept. 2012, 2013, and 2014), HS3 obtained observations over 9 named storms during 21 flights, along with additional flights over SAL outbreaks and non-developing systems. HS3 demonstrated a key component of the observing system envisioned by MacDonald (2005) by bringing to bear the high-altitude long-endurance GH platform, a broad array of instruments, and new sampling strategies to provide data for in-depth study, for assimilation into models, and for detailed evaluation and validation of models.

## **AIRCRAFT**

HS3 utilized two of NASA's unmanned GH aircraft [see Braun et al. (2013) for a background on the aircraft] and selected distinct payload sets for each aircraft. One GH, known as air vehicle one (AV-1) because it was the first GH ever built, was designated the "over-storm GH" since it carried three instruments specifically designed to measure the inner-core structure of storms. The second GH, known as AV-6, was designated the "environmental GH" because it carried instruments designed to characterize the storm environment including temperature, relative humidity, wind speed and direction, and profiles of Saharan dust. Unfortunately, due to engine and electrical issues, AV-1 was unable to deploy to the field in 2012 and 2014. In 2014, when it became clear that AV-1 would not deploy, the High-altitude Imaging Wind and Rain Airborne Profiler (HIWRAP) radar and Hurricane Imaging Radiometer (HIRAD) (see Braun et al. 2013 for descriptions) were moved onto the NASA Johnson Space Center WB-57f, which was conducting a coincident Office of Naval Research (ONR) Tropical Cyclone Intensity (TCI) mission utilizing a newly developed dropsonde system. The WB-57f is capable of flight durations up to 6 hours, a range of approximately 3700 km, and altitudes of approximately 18.3 km (60,000 ft). Three science missions were flown by the WB-57f, which deployed from McDill Air Force Base near Tampa, Florida.

## **HS3 PAYLOADS**

The environmental GH carried three instruments, including the Scanning High-resolution Interferometer Sounder (S-HIS), Cloud Physics Lidar (CPL) and Airborne Vertical Atmospheric Profiling System (AVAPS).

S-HIS (details in Table 1; Revercomb 2015) is an advanced version of the HIS ER-2 instrument (Revercomb et al. 2003). Its noise levels are sufficiently low to allow cloud and surface properties to be derived from each individual field of view. Temperature and water vapor profiling can be performed on individual fields of view in the absence of significant clouds after taking advantage of Principal Component Analysis to reduce noise levels (Antonelli et al, 2004). The optical design is very efficient, providing useful signal-to-noise performance from a single 0.5-second dwell time. This allows imaging to be accomplished by cross-track scanning. Onboard reference blackbodies are viewed via a rotating 45° scene mirror as part of each cross-track scan, providing updated calibration information every 20-30 seconds.

CPL is a multi-wavelength backscatter lidar (McGill et al. 2002, 2003). CPL provides information on the radiative and optical properties of cirrus, subvisual cirrus clouds, and aerosols (McGill and Hlavka 2015). CPL utilizes a high-repetition rate, low-pulse energy transmitter and photon-counting detectors and measures the total (aerosol plus Rayleigh) attenuated backscatter as a function of altitude at each wavelength. For transmissive cloud/aerosol layers, the extinction-to-backscatter parameter (S-ratio) can be directly derived using optical depth measurements determined from attenuation of Rayleigh and aerosol scattering and using the integrated backscatter. This permits unambiguous analysis of cloud optical depth since only the lidar data is required. Using the derived extinction-to-backscatter ratio, the internal cloud extinction profile can then be obtained (McGill et al 2003).

The AVAPS dropsonde system has been used for hurricane research for several decades (Hock and Franklin 1999; Halverson et al. 2006). Dropsondes provide in-situ, high-vertical-resolution profiles of basic atmosphere state variables – temperature, pressure, humidity, location, and winds (Wick 2015). The GH dropsonde system was built by the National Center for

Atmospheric Research (NCAR) and carries up to 88 dropsondes per flight. In 2012, AVAPS experienced significant radio frequency interference (RFI) problems that resulted in the loss of data within a portion, and in some cases the majority, of some dropsonde profiles. The lowest levels were most frequently impacted. The RFI issues were resolved before the 2013 campaign.

The over-storm payload consisted of the High-altitude Atmospheric Monolithic Microwave Integrated Circuits Sounding Radiometer (HAMSR), HIWRAP, and HIRAD. A description of these instruments can be found in Braun et al. (2013).

## **SUMMARY OF HS3 FLIGHTS**

During the 3 years of deployments, HS3 flew 670 total flight hours and released 1426 dropsondes, including full 88-dropsonde loads on two flights (19-20 Sept. 2013 and 16-17 Sept. 2014). The GH flew 18 flights over 8 named storms over 3 years while the WB-57f flew 3 flights over Hurricane Gonzalo in 2014 (Table 2).

In addition, the GH flew 2 non-developing systems (19-20 Sept. 2013 and 5-6 Sept. 2014) that the National Hurricane Center (NHC) predicted had some potential to develop, 2 flights specifically targeting the SAL (20-21 and 24-25 Aug., 2013), and 2 broad surveys of the Atlantic Main Development Region (MDR) (22-23 and 28-29 Sept., 2014). Several additional flights focused on instrument inter-comparisons. The 8-9 Sept. 2011 flight sampled an atmospheric river event and was designed to inter-compare temperature and humidity profiles from AVAPS, HAMSR, and S-HIS. The 13-14 Sept. 2011 and 30 Sept. 2014 flights were designed to compare measurements from GH and National Oceanic and Atmospheric Administration (NOAA) G-IV dropsondes. The 25 Sept. 2013 flight sampled precipitation in a mid-latitude frontal system to compare measurements from the HIWRAP (GH) and IWRAP (NOAA P-3) radars. Flight tracks for all flights, excluding the instrument inter-comparison and test flights, are shown in Fig. 1.

The most significant storms of the campaign were hurricanes Nadine (2012), Edouard (2014), and Gonzalo (2014). Hurricane Nadine and Tropical Storm Gabrielle were the only tropical cyclones to involve significant SAL interactions. Edouard and Gonzalo were the only major hurricanes to occur during the 3 deployments. Hurricane Cristobal was sampled during its extratropical transition.

## SCIENCE HIGHLIGHTS

A number of future studies will provide detailed analyses of the observations obtained during HS3. This section provides highlights of notable events and unique opportunities for research enabled by the HS3 mission. The highlights include a period of apparent rapid intensification not noted in the final NHC Tropical Cyclone Report for Hurricane Edouard, eyewall replacement cycles in Hurricane Gonzalo, SAL interaction with Hurricane Nadine, and unprecedented storm outflow measurements.

### *Rapid intensification of Hurricane Edouard (2014)*

Four flights were conducted over Hurricane Edouard's lifecycle, including a period of rapid intensification on 14-15 September 2014. Key measurements from the first two flights are described below.

During HS3's first Edouard flight on 12 September, the GH was on station from approximately 0430 to 1430 UTC. Edouard, then a tropical storm with maximum winds  $\sim 18.0$ - $20.5 \text{ m s}^{-1}$  (35-40 kt), was experiencing moderate vertical wind shear ( $\sim 7.7 \text{ m s}^{-1}$ ). Analysis of the GH dropsondes showed a well-organized cyclonic circulation at 800 hPa (Fig. 2a) centered on a region of intense convection and with relatively moist environmental conditions ( $>70\%$ ) at most locations. The precipitation and cloud cover suggested a high degree of asymmetry



associated with the westerly to northwesterly vertical wind shear. At 400 hPa (Fig. 2b), strong west-northwesterlies brought very dry air over the southern portion of the storm, and the center of circulation was displaced ~200 km to the northeast of the low-level center. A well-defined outflow jet at 200 hPa (Fig. 2c) was evident on the northern side of the storm with anticyclonic flow near the center.

During the 14-15 September flight, Edouard became vertically aligned (Fig. 2d-e) as the vertical shear weakened. Although dry environmental air was present, particularly at mid-to-upper levels (Fig. 2e), Edouard intensified to  $41 \text{ m s}^{-1}$  (80 kt) by 0000 UTC 15 September according to the NHC final report (Stewart 2014) and developed a broad outflow jet at 200 hPa on the western side of the storm (Fig. 2f) while maintaining a well-defined cyclonic circulation close to the center.

During this second flight, the NHC rejected many of the AVAPS dropsonde observations of surface pressure in the eye and eyewall, believing them to be too low compared to expected values estimated from other sources. Here, we provide evidence to suggest that a brief period of rapid intensification occurred over a 9-hour stretch, followed by a period of weakening as the small eye broke down and reformed into a much larger eye as a result of an apparent eyewall replacement cycle.

Dropsondes from the NOAA P-3 (NOAA43) and the GH provide estimates of Edouard's intensity as measured by the storm's minimum central pressure. Table 3 lists data from 5 dropsondes released in the vicinity of the eye or inner edge of the eyewall during the period from 1500 UTC 14 September to 0430 UTC 15 September (2 dropsondes from the NOAA P-3 and 3 from the GH). All of the dropsondes, except the first P-3 drop, also measured strong surface winds up to  $44 \text{ m s}^{-1}$ , suggesting that the dropsondes entered the low-level eyewall before

reaching the surface. The minimum central pressure of the storm is estimated by reducing the dropsonde derived surface pressure 1 hPa per  $5.1 \text{ m s}^{-1}$  (10 kt) of wind speed (R. Pasch, NHC, personal communication). Figure 3 shows the distribution of GH dropsondes in the inner-core region from the entire flight, with dropsonde locations adjusted for storm motion and dropsonde drift to a reference time of 0032 UTC 15 September (the time of the second center drop during the GH flight). The lowest surface pressures and strongest winds were near the northern eyewall, with weaker winds and higher pressures near the southern eyewall. Although the surface pressures in the northern eyewall were lower than NHC estimates, there is consistency in the low-pressure values that suggests valid measurements rather than spurious values.

The onset of Edouard's rapid intensification during this 14 September flight is consistent with satellite imagery and NOAA P-3 dropsondes.

- 0845 UTC: An initial eye became apparent in GOES infrared imagery around.
- 1115 UTC: A convective burst developed on the northwestern side of the eye, moved around to the southern side and expanded to the point of obscuring the eye (Fig. 4a-b).
- 1500 UTC: As the cloud shield from the convective burst began to wrap around to the eastern side of the circulation (1515 UTC, Fig. 4c), a NOAA P-3 dropsonde measured a central pressure of 983 hPa with low wind speeds (Table 3), suggesting a dropsonde very near the center.
- 1707 UTC: A P-3 dropsonde on the inner edge of the northeastern eyewall measured a surface pressure of 984 hPa and a surface wind of  $41 \text{ m s}^{-1}$ . Reducing the minimum surface pressure estimate by 8 hPa gives a central pressure of 976 hPa, a 7-hPa decrease from just two hours earlier.

- 1715 UTC: A new, very small eye formed in the GOES imagery (Fig. 4d), suggesting the onset of upper-level descent in the eye. Therefore, there is evidence of the onset of rapid intensification in the P-3 and GOES data even before consideration of the GH data.

During the period when Edouard had a very small eye (1715-0215 UTC), the GH released 2 dropsondes in the eye that entered the eyewall at low levels on the northern side of the eyewall. The first GH center transect was a north-to-south pass, with the eye overflight occurring near 2104 UTC 14 September (Fig. 5a). GOES IR imagery (Fig. 4e) showed a very small eye with the GH passing between two regions of higher cloud-top heights (inferred from the colder cloud-top temperatures) associated with deep convection. Brightness temperatures from S-HIS (Fig. 5a) indicated that the 2104 UTC dropsonde was released on the eastern side of the eye, with the dropsonde gradually moving around to the northern eyewall at low levels. This dropsonde measured a surface pressure of 971.7 hPa and an estimated 10-m wind speed of  $41.7 \text{ m s}^{-1}$  (81 kt). Adjusting for the high wind speed gives a central pressure estimate of 963.6 hPa, suggesting a  $\sim 13$ -hPa drop in pressure in 4 hours since the last P-3 drop and a 19-hPa drop since 1500 UTC.

Although the GOES imagery suggested significant axisymmetrization of the cloud field during RI, the storm circulation remained highly asymmetric. Figure 5b shows a vertical cross section of storm-relative tangential winds obtained from dropsondes along this north-to-south flight leg, with the 2104 UTC dropsonde closest to the storm center. The dropsonde spacing in the inner-core region was insufficient to resolve the eyewall and eye, but the figure clearly shows the strong tangential winds on both the northern and southern sides of the center. Strong radial inflow (Fig. 5c) occurred in the boundary layer on the northern side of the storm while weak

outflow was present south of the center. A prominent outflow jet was present in the 8.5-15 km altitude layer to the north of the center, while weaker outflow near 11 km altitude occurred to the south, consistent with the 200-hPa wind analysis in Fig. 2f. Dry air (Fig. 5d) was located about 2° (~200 km) to the south and 3° (~300 km) to the north of the center of the storm<sup>1</sup>.

During the second center overflight at 0032 UTC 15 September (see corresponding GOES imagery for 0045 UTC in Fig. 4f), a dropsonde released in the upper eye fell into the northern eyewall at low levels, measuring a surface pressure of 967.2 hPa and a near-surface wind of 44 m s<sup>-1</sup> (86 kt), suggesting an estimated central pressure of 958.6 hPa. Figure 6 shows the timing of the 0032 UTC dropsonde relative to the cloud attenuated backscatter from CPL and real-time temperatures from S-HIS. The 0032 UTC dropsonde was clearly released into the eye and the CPL (Fig. 6) and dropsonde data (not shown) both suggest that the dropsonde entered the inner edge of the eyewall near 800 hPa.

Edouard's small eye persisted continuously in GOES imagery until 0215 UTC, after which time the cloud structure gradually became more disorganized (Fig. 4g-h), suggesting a reorganization of the eyewall. By 0900 UTC, a new eye reformed in the upper-level clouds (shown in Fig. 4i at 1345 UTC), but with a much larger radius (~0.9°) than seen earlier (~0.2°, Fig. 4e). The last GH dropsonde near the center at 0428 UTC measured a higher pressure in the northern eyewall area (estimated central pressure of 963 hPa), suggesting a weakened intensity coincident with the apparent eyewall replacement cycle.

Based upon the P-3 and GH dropsondes, an estimated time series of minimum central pressure is shown in Fig. 7 along with the NHC best-track pressures (Stewart 2014). The aircraft

---

<sup>1</sup> Comparisons between S-HIS and AVAPS suggest a dry bias in the AVAPS data above 400 hPa, so relative humidities with respect to ice above ~8 km should be closer to saturation within the cloud system.

data, combined with the GOES imagery, suggest that during the period of the P-3 flight and the first half of the GH flight, Edouard transitioned from an asymmetric system during a major convective burst to a more symmetric system (in the GOES cloud-top field, but not the wind field; Fig. 5) with a well-defined but very small eye, and that during this time rapid intensification occurred as the central pressure decreased from 983 to 958 hPa. This short-duration RI phase suggests a brief period at near category-3 intensity compared to the best-track time series and could not be detected by the once-a-day NOAA P-3 flights<sup>2</sup>, indicating the added value of the long-duration GH. The 0032 UTC dropsonde-derived central pressure is consistent with, but somewhat lower than, some of the satellite-based intensity estimates (red dots) in Fig. 7. The intensification just as quickly came to an end when the initially small eye broke down and got replaced by a much larger eye. Intensification resumed with the formation of the new and larger eye, leading to a second period of category-3 intensity.

#### *Tropical Cyclone-SAL interaction (Nadine)*

Hurricane Nadine (2012) was HS3's best case for examining the interaction of a tropical cyclone with the SAL. Nadine originated from a tropical wave that emerged from the West African coast on 7 September in association with a small dust outbreak to its north. As the wave moved westward on 9 September, a large and more intense dust outbreak exited the Sahara and advanced toward the tropical disturbance. Nadine became a tropical depression on 10 September (Fig. 8a) and by 11 September (Fig. 8b) the SAL outbreak was encroaching on the cloud system's northern and eastern sides. Nadine became a tropical storm at 0000 UTC 12 September during the middle of the first GH flight. Dropsonde data were collected in the western part of the

---

<sup>2</sup> There were no Air Force Hurricane Hunter flights during Edouard.

storm, but were discontinued midway through the flight after a dropsonde became jammed in the launcher. As a result, no dropsondes were obtained in the eastern part of the storm and within the SAL.

Neither dropsonde nor CPL data indicated the presence of SAL air in the northwestern quadrant of the storm during the 11-12 September flight (northern portions of the 2<sup>nd</sup> and 3<sup>rd</sup> flight legs from the left on the western side of the storm in Fig. 8b). With dropsondes disabled, CPL and S-HIS detected a deep layer of SAL air (Fig. 9) along the northern portions of the 4<sup>th</sup> and 5<sup>th</sup> flight legs in Nadine's northeastern quadrant. Upon traversing north of Nadine's upper cloud shield (~0100 UTC, Fig. 9a), CPL detected a deep dust layer with a top near 530 hPa. In the dust region, S-HIS retrievals (Fig. 9b) indicated very hot and dry (0-20% relative humidity) air between 850-700 hPa and cooler and more moist conditions (~50%) near the top of the dust layer, consistent with Carlson and Prospero (1972), Messenger et al. (2009), Ismail et al. (2010), and Braun (2010).

The 14-15 September flight occurred as Nadine was moving northward near 54°W with the SAL encroaching on its eastern and northern sides (Fig 8c-e). Vertical shear estimates from the Statistical Hurricane Intensity Prediction System (SHIPS, DeMaria and Kaplan 1994, 1999; DeMaria et al. 2005) indicated 850-200 hPa vertical wind shear (not shown) changing from weak northwesterly shear on 12 September to west-southwesterly shear of 12-15 m s<sup>-1</sup> by 0000 UTC 15 September. During the period of weak shear on 12 September, Nadine intensified 12.9 m s<sup>-1</sup> in 24 hours, 2.6 m s<sup>-1</sup> below the threshold for rapid intensification (Kaplan and DeMaria 2003). With the onset of stronger vertical shear on 13 September, negligible intensification occurred from 0000 UTC 13 to 1200 UTC 14 September. A series of convective bursts and coincident frequent lightning during the GH flight between 1400-2100 UTC 14 September helped Nadine

just reach hurricane intensity by 1800 UTC 14 September before strong environmental westerlies pushed Nadine quickly eastward over cooler waters.

Global Hawk dropsonde observations of equivalent potential temperature ( $\theta_e$ ) and storm-relative winds spanning the period 17 UTC 14 September to 08 UTC 15 September are shown in Fig. 10. At 800 hPa (Fig. 10a), low  $\theta_e$  air associated with the SAL is found on the eastern side of the storm wrapping around the northern side, consistent with MODIS observations over preceding days, with a principal rainband marking the boundary between SAL in the outer environment and more moist conditions in the inner core. The dry SAL air is on the downshear side of the storm and so may have had a pathway into the inner-core circulation on the north (downshear) side of the storm (Willoughby et al. 1984; Marks et al. 1992; Braun et al. 2006; Riemer and Montgomery 2011). At 400 hPa (Fig. 9b), very dry westerly flow associated with the strong environmental shear impinged on the entire western flank of the storm, with the driest air wrapping around the southern side of the circulation. It is not yet possible to determine the impact of the SAL and upper-level dry air from these observations. However, ensemble simulations with the Weather Research and Forecasting model with coupled aerosol-cloud-radiation physics are being used to quantify the role of the SAL and dry air in this case.

#### *Tropical cyclone outflow structure*

Tropical cyclone outflow is a prominent part of the secondary circulation and its thermodynamic structure plays a key role in hurricane maximum potential intensity (MPI) theory. Emanuel (1986, 1997) derived expressions for MPI that depended on a constant outflow temperature with the outflow occurring above the tropopause (Emanuel and Rotunno 2011). The model assumed that outflow streamlines asymptotically approach altitudes at which their

saturated entropy values match those of the undisturbed environment so that outflow structure is determined by environmental stratification. However, Emanuel and Rotunno (2001) used simulated storms to demonstrate that outflow stratification is instead the result of internal dynamics and small-scale turbulence that limits the Richardson number ( $Ri$ ) to a critical value needed for the onset of that turbulence.

Molinari et al. (2014) examined NOAA G-IV dropsonde data and identified three situations that produce low  $Ri$  in outflow regions. The first situation was just beneath the outflow-layer stratiform cloud deck where sublimation cooling produced high stability near cloud base and a neutral or unstable lapse rate and low  $Ri$  just beneath the stable layer. In the second case, low  $Ri$  occurred above cloud base where radiative heating (cooling) near cloud base (top) resulted in sufficiently low stability to cause low  $Ri$  values. Vertical wind shear was not a contributor to the low  $Ri$  in either of these cases. The third situation occurred outside the central dense overcast in association with strong vertical wind shear at the base of the outflow layer.

The G-IV dropsondes typically provide data only below 12-13 km and therefore miss the upper part of the outflow layer and the lower stratosphere. During HS3, the GH provided relatively high-density coverage over a large extent of the outflow layer from the lower stratosphere to the surface. An example of outflow layer structure was shown in Fig. 5. To the north of the center, outflow  $>4 \text{ m s}^{-1}$  extended vertically between  $\sim 8.5$  to 15 km and from the eyewall to more than  $8^\circ$  ( $\sim 770 \text{ km}$ ) from the center. The strongest outflow occurred just beneath cloud top near the northern eyewall, but beyond a radius of  $\sim 200 \text{ km}$ , outflow often extended above and beyond regions of cloudiness. In addition to inflow beneath the outflow layer, another region of strong inflow existed in the lower stratosphere above the outflow layer and extended all the way inward to the storm center. Tangential velocities in the outflow layer transitioned from



cyclonic flow beneath cloud top out to  $\sim 28^\circ\text{N}$  ( $\sim 250$  km radius) to strong anticyclonic flow northward of  $30^\circ\text{N}$  ( $\sim 400$  km radius). A very shallow layer of strong anticyclonic velocities occurred at the tropopause at the transition from upper-tropospheric outflow to lower-stratospheric inflow.

Figure 11 shows results from a calculation of the Richardson number using the data shown in Fig. 5. In unsaturated regions (taken here as regions with relative humidity  $< 95\%$ ),  $Ri$  is estimated from  $Ri = N^2/S^2$ , where  $N^2 = (g/\theta_v)(\Delta\theta_v/\Delta z)$ ,  $S^2 = [(\Delta U)^2 + (\Delta V)^2]/(\Delta z)^2$ ,  $\theta_v$  is the virtual potential temperature,  $U$  and  $V$  are the zonal and meridional wind components, respectively, and  $z$  is geopotential height. Where relative humidity  $> 95\%$ , a moist  $Ri$  [Eqs. A1-A4 of Molinari et al (2014)] derived from Durran and Klemp (1982) is used. In addition to the very low moist  $Ri$  values in the inner core below 6 km associated with both low stability ( $N^2$ , Fig. 11b) and moderate shear ( $S$ , Fig. 11c), very low  $Ri$  ( $< 0.25$ ) are found primarily above the outflow layer just above the tropopause. This layer is characterized by high stability and very strong shear, the latter being responsible for the low  $Ri$  values. This layer of low  $Ri$  would not be detectable from G-IV dropsondes because of their lower release altitude. The dropsonde profiles near  $23.7^\circ$  (at 6- and 7.5-km altitude) and  $29.7^\circ\text{N}$  (at 7 km) exhibit sublimation-induced unstable layers a few hundred meters in depth associated with intrusions of dry air beneath cloud base at mid levels similar to that seen by Molinari et al. (2014). Within the outflow layer, some regions with  $Ri < 1$  are found, particularly near the northern eyewall, and are often associated with low stability in the outflow layer. However, unlike in Molinari et al. (2014), moderate vertical wind shear usually also contributes significantly to the low  $Ri$  values there.

## SUMMARY

Along with the NASA GRIP campaign, HS3 has demonstrated the unique contributions of the Global Hawk for conducting hurricane science research, taking advantage of the long duration, high altitude, and heavy payload capabilities of the aircraft. While GRIP produced the first-ever GH flights, the GH was launched from NASA's Armstrong Flight Research Center in Southern California, which greatly reduced on-station times for storms eastward of the Gulf of Mexico and prevented flights east of about 66°W. HS3 paved the way for flights from the East Coast and demonstrated the use of mobile trailers for controlling the GH and its payload. These East Coast deployments allowed flights of most systems in the Atlantic, particularly for storms not accessible by operational manned aircraft. HS3 also showed that the GH can conduct surveillance over extended periods of any tropical weather system in the Atlantic/Caribbean basin. Tasking of the UAS can also be adjusted in real-time to account for changing storm conditions.

Over the course of the HS3 mission, NASA developed key relationships with NOAA, the Federal Aviation Administration, and Department of Defense to implement and improve operational procedures and demonstrate the scientific value of the GH data sets, leading to efforts by NOAA's Sensing Hazards with Operational Unmanned Technologies (SHOUT) program to examine the operational forecasting utility of the GH platform and instruments.

## *Acknowledgements*

The HS3 mission was funded by NASA's Earth Venture Suborbital program at NASA Headquarters. NOAA P-3 dropsonde data were provided by NOAA's Physical Oceanography Division (PHOD) of Atlantic Oceanographic and Meteorological Laboratory. Dennis Hlavka and

390 John Yorks from Goddard provided the CPL data. Peter Black, James Doyle, and Jon Moskaitis  
391 provided valuable discussions related to storm outflow.

392

### **Sidebar: Inner-Core Structure During Hurricane Gonzalo.**

The three flights of the WB-57f over Hurricane Gonzalo (Fig. 1d and Table 2) provided inner-core measurements during an interesting period when the storm was moving northwestward and then north-northeastward around a ridge in the central Atlantic. The storm intensified from category 3 on 15 October to category 4 on 16 October, when it had a minimum central pressure of 940 hPa and maximum winds of 125 kt. An eyewall replacement cycle occurred on the 15<sup>th</sup>, causing the storm to weaken briefly before recurving. Gonzalo again had a double eyewall late on 16 October, also concurrent with a weakening of the storm.

Figure S1 shows the HIWRAP (Heymsfield 2015) reflectivity structure highlighting the double eyewall structure on 17 September 2014. Gonzalo had an asymmetrical structure with its cloud shield spreading to the north and east. The heavier precipitation in the cross section is on the northwest side of the storm. This cross section and other similar passes over the three days are being analyzed for both precipitation and wind structure similar to what has been done in previous HIWRAP studies (Guimond et al. 2014; Didlake et al. 2014).

## References

- Braun, S. A., 2010: Re-evaluating the role of the Saharan Air Layer in Atlantic tropical cyclogenesis and evolution. *Mon. Wea. Rev.*, **138**, 2007-2037.
- Braun, S. A., M. T. Montgomery, and Z. Pu, 2006: High-Resolution Simulation of Hurricane Bonnie (1998). Part I: The Organization of Vertical Motion. *J. Atmos. Sci.*, **63**, 19-42.
- Braun, S. A., and coauthors, 2013: NASA's Genesis and Rapid Intensification Processes (GRIP) Field Experiment. *Bull. Amer. Meteor. Soc.*, **94**, 345-363.
- Carlson, T.N., and J.M. Prospero, 1972: The large-scale movement of Saharan air outbreaks over the northern equatorial Atlantic. *J. Appl. Meteor.*, **11**, 283-297.
- DeMaria, M., and J. Kaplan, 1994: A Statistical Hurricane Intensity Prediction Scheme (SHIPS) for the Atlantic basin. *Wea. Forecasting*, **9**, 209-220.
- DeMaria, M., and J. Kaplan, 1999: An updated statistical hurricane intensity prediction scheme (SHIPS) for the Atlantic and eastern North Pacific Basins. *Wea. Forecasting*, **14**, 326-337.
- DeMaria, M. M. Mainelli, L. K. Shay, J. A. Knaff, and J. Kaplan, 2005: Further Improvements to the Statistical Hurricane Intensity Prediction Scheme (SHIPS). *Wea. Forecasting*, **20**, 531-543.
- Didlake, A. C., Jr., G. M. Heymsfield, L. Tian, and S. R. Guimond, 2015: The coplane analysis technique for three-dimensional wind retrieval using the hiwrap airborne doppler radar. *J. Appl. Meteor. Climatol.*, **54**, 605-623. doi: <http://dx.doi.org/10.1175/JAMC-D-14-0203.1>
- Durrán, D. R., and J. B. Klemp, 1982: On the effects of moisture on the Brunt-Väisälä frequency. *J. Atmos. Sci.*, **39**, 2152-2158
- Emanuel K. A., 1986: An air-sea interaction theory for tropical cyclones. Part I: Steady-state

433 maintenance. *J. Atmos. Sci.*, **43**, 585–604.

434 Emanuel, K. A., 1997: Some aspects of hurricane inner-core dynamics and energetics. *J.*  
 435 *Atmos. Sci.*, **54**, 1014–1026.

436 Emanuel, K. A., and R. Rotunno, 2011: Self-stratification of tropical cyclone outflow. Part I:  
 437 Implications for storm structure. *J. Atmos. Sci.*, **68**, 2236–2249, doi:[10.1175/JAS-D-10-](https://doi.org/10.1175/JAS-D-10-05024.1)  
 438 [05024.1](https://doi.org/10.1175/JAS-D-10-05024.1).

439 Guimond, S. R., L. Tian, G. M. Heymsfield, and S. J. Frasier, 2014: Wind retrieval algorithms  
 440 for the IWRAP and HIWRAP airborne Doppler radars with applications to hurricanes. *J.*  
 441 *Atmos. Oceanic Technol.*, **31**, 1189–1215.

442 Halverson, J. B., J. Simpson, G. Heymsfield, H. Pierce, T. Hock, and L. Ritchie, 2006: Warm  
 443 core structure of Hurricane Erin diagnosed from high-altitude dropsondes during  
 444 CAMEX-4. *J. Atmos. Sci.*, **63**, 309–324.

445 Heymsfield, Gerald H. 2015. Hurricane and Severe Storm Sentinel (HS3) High Altitude Imaging  
 446 Wind and Rain Airborne Profiler (HIWRAP). Dataset available online  
 447 [<https://hs3.nsstc.nasa.gov/pub/hs3/HIWRAP/>] from the NASA Global Hydrology Resource  
 448 Center DAAC, Huntsville, Alabama,  
 449 U.S.A. <http://dx.doi.org/10.5067/HS3/HIWRAP/DATA101>

450 Hock, T., and J. L. Franklin, 1999: The NCAR GPS dropwindsonde. *Bull. Amer. Meteor. Soc.*,  
 451 **80**, 407–420.

452 Ismail, S., and coauthors, 2009: LASE measurements of water vapor, aerosol, and cloud  
 453 distributions in Saharan air layers and tropical disturbances. *J. Atmos. Sci.*, **67**, 1026–  
 454 1047.

455 Kaplan, J., and M. DeMaria, 2003: Large-scale characteristics of rapidly intensifying tropical  
 456 cyclones in the North Atlantic basin. *Wea. Forecasting*, **18**, 1093-1108.

457 MacDonald, A. E., 2005: A global profiling system for improved weather and climate  
 458 prediction. *Bull. Amer. Meteor. Soc.*, **86**, 1747-1764.

459 Marks, F. D., Houze, R. A., and Gamache, J. F., 1992: Dual-aircraft investigation of the inner  
 460 core of Hurricane Norbert. Part I: Kinematic structure, *J. Atmos. Sci.*, **49**, 919-942.

461 McGill, Matthew and Dennis Hlavka. 2015. Hurricane and Severe Storm Sentinel (HS3) Global  
 462 Hawk Cloud Physics Lidar (CPL) [ATB files]. Dataset available online  
 463 [<https://hs3.nsstc.nasa.gov/pub/hs3/CPL/>] from the NASA Global Hydrology Resource  
 464 Center DAAC, Huntsville, Alabama, U.S.A.  
 465 doi: <http://dx.doi.org/10.5067/HS3/CPL/DATA202>.

466 McGill, M., D. Hlavka, W. Hart, V. S. Scott, J. Spinhirne, and B. Schmid, 2002: Cloud Physics  
 467 Lidar: Instrument Description and Initial Measurement Results. *Appl. Opt.*, **41**, 3725-  
 468 3734.

469 McGill M., L. Li, W. D. Hart, G. M. Heymsfield, D. L. Hlavka, P. E. Racette, L. Tian, M. A.  
 470 Vaughan, and D. M. Winker, 2003: Combined lidar-radar remote sensing: Initial results  
 471 from CRYSTALFACE. *J. Geophys. Res.*, **109**, D07203, doi: 10.1029/2003JD004030.

472 Messenger, C., D. J. Parker, O. Reitebuch, A. Agusti-Panareda, C. M. Taylor, and J. Cuesta, 2009:  
 473 Structure and dynamics of the Saharan atmospheric boundary layer during the West  
 474 African monsoon onset: Observations and analyses from the research flights of 14 and  
 475 17 July 2006. *Quart. J. Roy. Meteor. Soc.*, **135**, doi:10.1002/qj.469.

476 Molinari, J., P. Duran, and D. Vollaro, 2014: Low Richardson Number in the Tropical Cyclone  
 477 Outflow Layer. *J. Atmos. Sci.*, **71**, 3164-3179.

478 Pielke, R. A., J. Gratz, C. W. Leadsea, D. Collins, M. A. Saunders, and R. Musulin, 2008:  
 479 Normalized hurricane damages in the United States: 1900–2005. *Natural Hazards*  
 480 *Review*, **9**, 29-42.

481 Revercomb, Henry. 2015. Hurricane and Severe Storm Sentinel (HS3) Scanning High-  
 482 Resolution Interferometer Sounder (S-HIS)). Dataset available online  
 483 [<https://hs3.nsstc.nasa.gov/pub/hs3/SHIS/>] from the NASA Global Hydrology Resource  
 484 Center DAAC, Huntsville, Alabama, U.S.A.  
 485 doi: <http://dx.doi.org/10.5067/HS3/SHIS/DATA201>.

486 Revercomb, H. E., and coauthors, 2003: Applications of high spectral resolution FTIR  
 487 observations demonstrated by radiometrically accurate ground-based AERI and  
 488 Scanning HIS aircraft instruments. SPIE Proceedings Multispectral and Hyperspectral  
 489 Remote Sensing Instruments and Applications, *Proc. SPIE*, 4897, **11**;  
 490 doi:10.1117/12.466834, 11–23.

491 Riemer, M., and M. T. Montgomery, 2011: Simple kinematic models for the environmental  
 492 interaction of tropical cyclones in vertical wind shear. *Atmos. Chem. Phys.*, **11**, 9395–  
 493 9414, doi:[10.5194/acp-11-9395-2011](https://doi.org/10.5194/acp-11-9395-2011).

494 Rogers, R., S. and coauthors, 2006: The Intensity Forecasting Experiment: A multi-year field  
 495 program for improving tropical cyclone intensity forecasts. *Bull. Amer. Meteor. Soc.*, **87**,  
 496 1523-1537.

497 Stewart, S. R., 2014: Hurricane Edouard (AL062014). NHC Tropical Cyclone Report, 19 pp.,  
 498 available at <http://www.nhc.noaa.gov/data/#tcr>.

499 Wick, Gary. 2015. Hurricane and Severe Storm Sentinel (HS3) Global Hawk AVAPS  
 500 Dropsonde System. Dataset available online [<https://hs3.nsstc.nasa.gov/pub/hs3/AVAPS/>]



501 from the NASA Global Hydrology Resource Center DAAC, Huntsville, Alabama,  
502 U.S.A. doi: <http://dx.doi.org/10.5067/HS3/AVAPS/DROPSONDE/DATA201>.  
503 Willoughby, H. E., F. D. Marks, and R. J. Feinberg, 1984: Stationary and moving convective  
504 bands in hurricanes. *J. Atmos. Sci.*, **41**, 3189–3211, doi:[10.1175/1520-](https://doi.org/10.1175/1520-0469(1984)041,3189:SAMCBI.2.0.CO;2)  
505 [0469\(1984\)041,3189: SAMCBI.2.0.CO;2](https://doi.org/10.1175/1520-0469(1984)041,3189:SAMCBI.2.0.CO;2).  
506

## Table Captions

Table 1. Instrument characteristics for the environmental and over-storm GH payloads.

Table 2. Summary of HS3 flights. AV=Air Vehicle. TS=Tropical Storm. TD=Tropical Depression. ET=Extratropical. NPP=NPOES Preparatory Project. MDR=Main Development Region.

Table 3. NOAA P-3 and NASA GH dropsonde data near or within the eye of Edouard during 14-15 September. Estimates of the minimum sea-level pressure at the storm center are obtained by reducing the observed surface pressure by 1 hPa per  $5.1 \text{ m s}^{-1}$  of 10-m level wind speed. Wind speeds are reduced to 10 m following Table 3 of Franklin et al. (2003).

## Figure Captions

Figure 1. Graphic summary of the HS3 Atlantic tropical cyclone and SAL flights. Panels show GH flight tracks for the (a) 2012 campaign, (b) 2013 campaign, and (c) 2014 campaign, while (d) shows the 2014 WB-57f flight tracks over Hurricane Gonzalo.

Figure 2. (a and b) Dropsonde-derived 800 hPa and 400 hPa relative humidity and (c) 200 hPa ground-relative wind speed (colored circles) from the 11-12 September 2014 flight. Color bars for relative humidity and wind speed are shown along the bottom of the figure. Wind barbs (full barb,  $5 \text{ m s}^{-1}$ ; half-barb,  $2.5 \text{ m s}^{-1}$ ; flags,  $25 \text{ m s}^{-1}$ ) show storm-relative winds at the respective altitudes. Dropsonde locations account for dropsonde drift and storm motion, with positions adjusted to a reference time of 0900 UTC 12 September. Data superimposed on GOES infrared imagery (IR) at 0845 UTC and SSMI/S 91 GHz polarization corrected temperature [color scale in (b)] at 0849 UTC 12 September. (d-f) Same as (a-c), but for a reference time of 0032 UTC 15 September and superimposed on GOES IR imagery at 0045 UTC 15 September. Satellite imagery is from the Naval Research Laboratory Tropical Cyclone web page (<http://www.nrlmry.navy.mil/TC.html>).

Figure 3. Plots of (a) surface pressure and (b) estimated 10-m ground-relative wind speed for the 14-15 September 2014 GH flight. Wind barbs (full barb,  $5 \text{ m s}^{-1}$ ; half-barb,  $2.5 \text{ m s}^{-1}$ ; flags,  $25 \text{ m s}^{-1}$ ) show storm-relative winds. Dropsonde positions are adjusted to a reference time of 0032 UTC 15 September using the observed position and time of the near-surface observations and an estimated storm motion based on the NHC-determined best track information.

541 Figure 4. GOES Infrared imagery (see color scale at bottom) from the Naval Research  
542 Laboratory tropical cyclone website for (a) 1115, (b) 1315, (c) 1515, (d) 1715, and (e) 2115 UTC  
543 14 September; and (f) 0045, (g) 0315, (h) 0715, and (i) 1315 UTC 15 September 2014.

544 Figure 5. (a) S-HIS brightness temperatures (color shading, K) for the  $895\text{-}900\text{ cm}^{-1}$  channel. The  
545 eye of Edouard is labeled “Eye” near the warm brightness temperatures associated with the low  
546 clouds in the eye. The black dashed line shows the approximate flight path (line segments  
547 through dropsonde points only). Short curved line segments indicate dropsonde horizontal  
548 trajectories, with the release point coinciding with the flight path. Dropsonde times (UTC) are  
549 indicated. (b) Tangential velocity, (c) radial velocity, and (d) relative humidity with respect to  
550 water for temperatures  $\geq 273.15\text{K}$  and with respect to ice at colder temperatures (color shading)  
551 derived from dropsonde data between 1935-2207 UTC 14 September. Dropsonde locations are  
552 indicated by vertical lines. Grey shading in right panels shows CPL attenuated backscatter (ABS,  
553  $\text{km}^{-1}\text{ sr}^{-1}$ ) multiplied by 100. Vertical arrow in (b) indicates the location of the center dropsonde  
554 at 2104 UTC.

555 Figure 6. CPL attenuated backscatter ( $\times 100$ ) and S-HIS real-time retrieved air temperature for  
556 the period 0020-0045 UTC 15 September during a transit over the storm from northeast to  
557 southwest of the center. Vertical dashed line shows the location of the 0032 UTC 15 September  
558 dropsonde.

559 Figure 7. Time series of NHC best-track (black line) central pressure and operational intensity  
560 estimates (red circles, from satellite and aircraft). The blue line indicates estimated central  
561 pressures from P-3 (black circles) and GH (open circles) dropsondes. Orange and purple lines

along the bottom of the figure indicate on-station times for NOAA P-3s and GH, respectively. Text indicates significant events during storm evolution.

Figure 8. MODIS daily cloud and aerosol optical depth (colors) images show the evolution of the SAL outbreak near Hurricane Nadine on the indicated days. The flight track for the 11-12 September flight is shown in (b) and for the 14-15 September flight in (e). MODIS imagery obtained from the NASA Worldview web page (<https://earthdata.nasa.gov/labs/worldview/>).

Figure 9. (a) CPL aerosol backscatter ( $\times 100 \text{ km}^{-1} \text{ sr}^{-1}$ ) showing the dust layer north of Nadine along the northern portions of the 5<sup>th</sup> and 6<sup>th</sup> north-south oriented flight legs (from left to right in Fig. 8b) during the 11-12 September 2012 flight. S-HIS (b) relative humidity and (c) temperature perturbation for the same flight segment. Temperature perturbations are derived by removing the average temperature from 2000 UTC 11 September to 0600 UTC 12 September. The horizontal line marks the top of the dust layer, and the vertical lines separate times of nearly clear skies (0100-0149 UTC) from times with upper-level cloud cover. There is a reversal in the temperature anomalies below 400 hPa and much higher low-level relative humidity before 0100 UTC and after 0149 UTC, suggesting possible retrieval biases caused by upper-level clouds. Vertical arrows indicate the times of aircraft turns, first from northbound to eastbound, second from eastbound to southbound.

Figure 10. Equivalent potential temperature (colored circles) and storm-relative wind barbs (full barb,  $5 \text{ m s}^{-1}$ ; half-barb,  $2.5 \text{ m s}^{-1}$ ; flags,  $25 \text{ m s}^{-1}$ ) at (a) 800 hPa and (b) 400 hPa superimposed on the GOES infrared imagery at 0015 UTC 15 September 2012. Dropsonde locations account for dropsonde drift and storm motion, with positions adjusted to a reference time of 0000 UTC 15 September. Color bars indicate  $\theta_e$  values (K) corresponding to the dropsonde data in each panel.

Figure 11. Plots of (a) bulk Richardson number and CPL attenuated backscatter ( $\times 100 \text{ km}^{-1} \text{ sr}^{-1}$ ), (b) Brünt-Vaisala frequency,  $N^2 \text{ (s}^{-2}\text{)}$ , and (c) vertical wind shear,  $S \text{ (s}^{-1}\text{)}$ , for the Edouard cross section shown in Fig. 5. In (a), the 45% relative humidity contour is shown to indicate an approximate boundary of very dry air. In (b), contours are of potential temperature at 4 K intervals while in (c) contours show outflow regions with radial velocity at  $4 \text{ m s}^{-1}$  intervals starting at  $4 \text{ m s}^{-1}$ .

Figure S1. Hurricane Gonzalo on 17 September 2014 as observed from the HIWRAP Ka-band frequency as the storm was approaching Bermuda. Vertical cross section (top) and horizontal cross sections at 2.7, 5.0 and 7.3 km altitude (bottom panels) reconstructed from HIWRAP conical scanning outer beam. Both inner and outer eyewalls are observed at 110 and 160 km, and 40 and 250 km, respectively. The Ka-band data shown has higher resolution than the Ku-band and is more sensitive to light precipitation at upper levels in the eyewall, but suffers more attenuation in heavy rain near the surface.

599 **Table 1.** Instrument characteristics for the environmental and over-storm GH payloads.

600

Instrument	Spectral Bands	Spatial Resolution (FOV), Profile Resolution	Retrieved Measurement Precision	Data Products
Environmental Payload				
CPL	355, 532, and 1064 nm, with depolarization at 1064 nm	100 m, 30 m vertical	Optical depth, 11-25%	Profiles of calibrated attenuated backscatter; cloud/aerosol layer boundaries; cloud/aerosol optical depth, extinction, and depolarization; color ratio
AVAPS	N/A	N/A, 0.5 s vertical	N/A	Quality controlled vertical profiles of temperature, pressure, humidity, wind speed and direction
S-HIS	Continuous spectral coverage 3.3 to 16.7 $\mu\text{m}$ @ 0.5 $\text{cm}^{-1}$	0.1 radians (11 samples cross track), 1-3 km vertical	Temperature < 1K, water vapor < 15%	IR temperature spectra, IR cloud-top temperature, cloud- top height, optical depth, effective radius, water skin temperature. Atmospheric temperature and water vapor profiles in clear-sky conditions
Over-Storm Payload				
HAMSR	8 channels between 50-60 GHz, 10 between	2 km horizontal, 1-3 km vertical	2 K for temperature, 15% for water	Calibrated geolocated brightness temperatures; vertical profiles of temperature, water vapor,

	113-118 GHz, and 7 between 166-183 GHz		vapor, 25% for liquid water	and liquid water; precipitation structure
HIRAD	4, 5, 6, 6.6 GHz	Horizontal resolution of 1.6 km (6.6 GHz) to 2.5 km (4 GHz) at nadir from 20 km altitude	1-5 m s <sup>-1</sup> for wind speed	Brightness temperatures at 4 C- band frequencies; surface wind speed, rain rate
HIWRAP	13.35, 13.91, 33.72, 35.56 GHz	0.42 km (Ka) and 1.0 km (Ku) horizontal, 60 m vertical	Horizontal winds, < 2 m s <sup>-1</sup>	Calibrated reflectivity, platform- corrected Doppler velocity, surface return, 3-D reflectivity fields and horizontal winds, ocean surface winds

601

602



**Table 2. Summary of HS3 flights. AV=Air Vehicle. TS=Tropical Storm. TD=Tropical Depression. ET=Extratropical. NPP=NPOES Preparatory Project. MDR=Main Development Region.**

Date	GH	Storm/Event	Description/comments
<b>2011</b>			
8-9 Sep	AV-6	Pacific atmos. river	North-south cross section from 50° to 10°N along 154°W for intercomparison of AVAPS, S-HIS, and HAMSR.
13-14 Sep	AV-6	No storm	Intercomparison of AVAPS and NOAA G-IV dropsondes in warning area off Tampa, FL.
<b>2012</b>			
6-7 Sep	AV-6	Hurr. Leslie	Outflow structure of Leslie during transit to WFF.
11-12 Sep	AV-6	TS Nadine	Nadine became a TS with SAL air along northern side. AVAPS failed mid-way through flight. Reduced CPL sensitivity due to cold instrument temperature.
14-15 Sep	AV-6	Hurr. Nadine	Nadine became a hurricane in high-shear conditions, SAL air wrapped partly around northern side. Reduced CPL sensitivity due to cold instrument temperature.
19-20 Sep	AV-6	TS Nadine	Nadine weakened to TS strength near the Azores. CPL issue resolved.
22-23 Sep	AV-6	TS Nadine	Nadine became a TS again after 1 day post-tropical.
26-27 Sep	AV-6	TS Nadine	Nadine moved southward, convection intensified 2 days prior

Sep			to re-intensification to hurricane strength.
6 Oct	AV-6	No storm	Underflew both NPP and Aqua, no dropsondes available.
5-6 Nov	AV-1	ET Cyclone	Test flight of AV-1 in an extratropical cyclone in the Pacific.
<b>2013</b>			
20-21 Aug	AV-6	Ex-Erin/SAL	Environmental sampling of shallow former TS Erin and SAL air mass. AVAPS released only 15 of 44 planned drops after it lost power from the aircraft.
24-25 Aug	AV-6	SAL	SAL flight in weak African wave disturbance.
29-30 Aug	AV-6	Pre-Gabrielle	Pre-Gabrielle African wave with SAL air.
3-4 Sep	AV-1	Pre-Gabrielle	Measurement of convective structure of Pre-Gabrielle and adjacent convective disturbance.
4-5 Sep	AV-6	TS Gabrielle	Environmental sampling of TS Gabrielle and adjacent convective disturbance.
7-8 Sep	AV-6	Ex-Gabrielle	Potential redevelopment of former TS Gabrielle.
15-16 Sep	AV-1	Hurr. Ingrid	Precipitation/wind measurements in Hurr. Ingrid. Flight cut short due to cold fuel temperatures.
16-17 Sep	AV-6	TS Humberto	Redevelopment of TS Humberto. Hybrid low-level warm-core/upper-level cold-core structure observed.
19-20	AV-6	Invest A95L	Environmental measurements of Invest A95L that, despite a

Sep			good low-level circulation and moisture, failed to develop into a tropical depression.
25 Sep	AV-1	ET cyclone	Precipitation system sampling in coordination with NOAA43 for HIWRAP/IWRAP intercomparison.
<b>2014</b>			
26-27 Aug	AV-6	Hurr. Cristobal	AV-6 transit and science flight over Hurricane Cristobal.
28-29 Aug	AV-6	Hurr. Cristobal	Hurricane Cristobal extratropical transition.
2-3 Sep	AV-6	TS Dolly	TS Dolly just prior to landfall along Mexican coast.
5-6 Sep	AV-6	SAL A90L	Invest A90L and its interaction with the SAL.
11-12 Sep	AV-6	TD6/TS Edouard	TS stage with possible nascent eye. CPL data loss due to disk failure.
14-15 Sep	AV-6	Hurr. Edouard	Four overflights near the center, rapid intensification.
16-17 Sep	AV-6	Hurr. Edouard	Mature stage, beginning of secondary eyewall replacement.
18-19 Sep	AV-6	Hurr./TS Edouard	Rapid weakening just west of the Azores.
22-23 Sep	AV-6	MDR Survey	Box from 60° to 21.5°W, eastbound at 19°N, westbound at 14°N.

28-29 Sep	AV-6	MDR Survey	Zig-zag pattern between 55°-27°W, 13-18°N.
30 Sep	AV-6	No storm	Intercomparison of AVAPS and G-IV dropsondes and flight-level winds during GH transit to AFRC.
15 Oct.	WB- 57f	Hurr. Gonzalo	Two overpasses of Cat 3 intensity storm.
16 Oct.	WB- 57f	Hurr. Gonzalo	Three overpasses of Cat 4 intensity storm.
17 Oct.	WB- 57f	Hurr. Gonzalo	Two overpasses of Cat 3-4 intensity storm.

603

604

605

**Table 3. NOAA P-3 and NASA GH dropsonde data near or within the eye of Edouard during 14-15 September. Estimates of the minimum sea-level pressure at the storm center are obtained by reducing the observed surface pressure by 1 hPa per  $5.1 \text{ m s}^{-1}$  of 10-m level wind speed. Wind speeds are reduced to 10 m following Table 3 of Franklin et al. (2003).**

Aircraft/ Day/Time (UTC)	Release Location Relative to Storm Center	Psfc (hPa)	Wind Speed Closest to 10- m Level ( $\text{m s}^{-1}$ )	Geopotential Height of Wind (m)	Estimated 10- m Wind Speed ( $\text{m s}^{-1}$ )/(kt)	Estimated MSLP (hPa)
P3/14/1500	Eye center	982.8	2.6	9	2.6/5.1	982.8
P3/14/1707	NE eye/eyewall	984.3	41.0	10	41.0/79.7	976.3
GH/14/2104	E eye/eyewall	971.7	45.3	33	41.7/81.1	963.6
GH/15/0032	Eye center	967.2	44.2	8	44.2/86.0	958.6
GH/15/0428	SE eye/eyewall	970.7	43.0	10	43.0/83.6	962.3

606

607

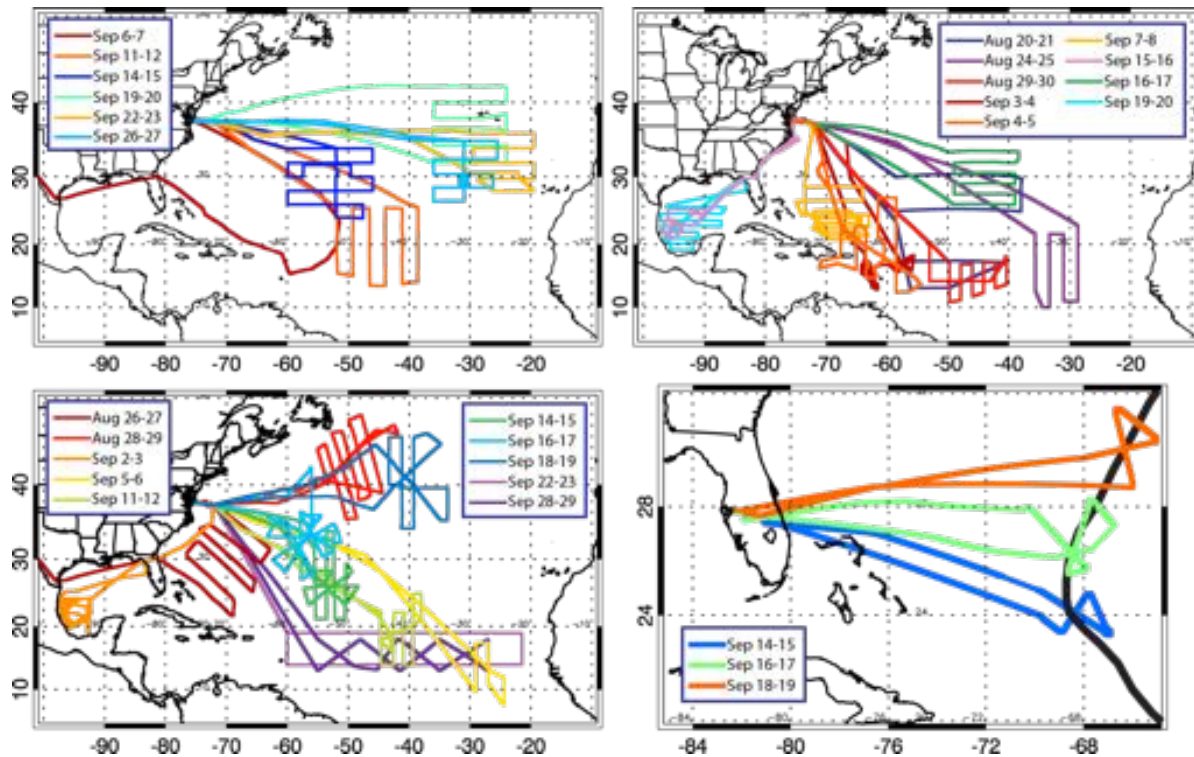
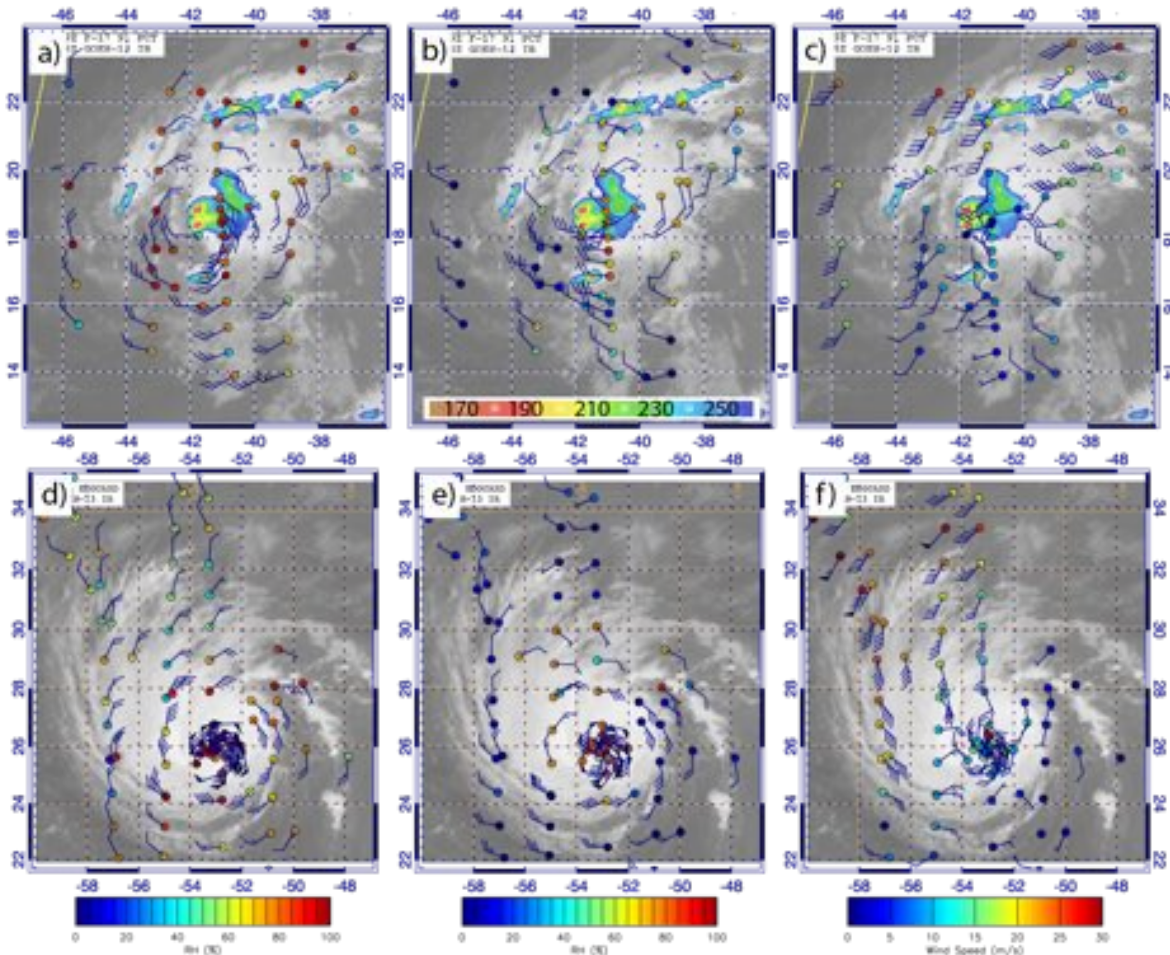


Figure 1. Graphic summary of the HS3 Atlantic tropical cyclone and SAL flights. Panels show GH flight tracks for the (a) 2012 campaign, (b) 2013 campaign, and (c) 2014 campaign, while (d) shows the 2014 WB-57f flight tracks over Hurricane Gonzalo.



613

614

615

616

617

618

619

620

621

622

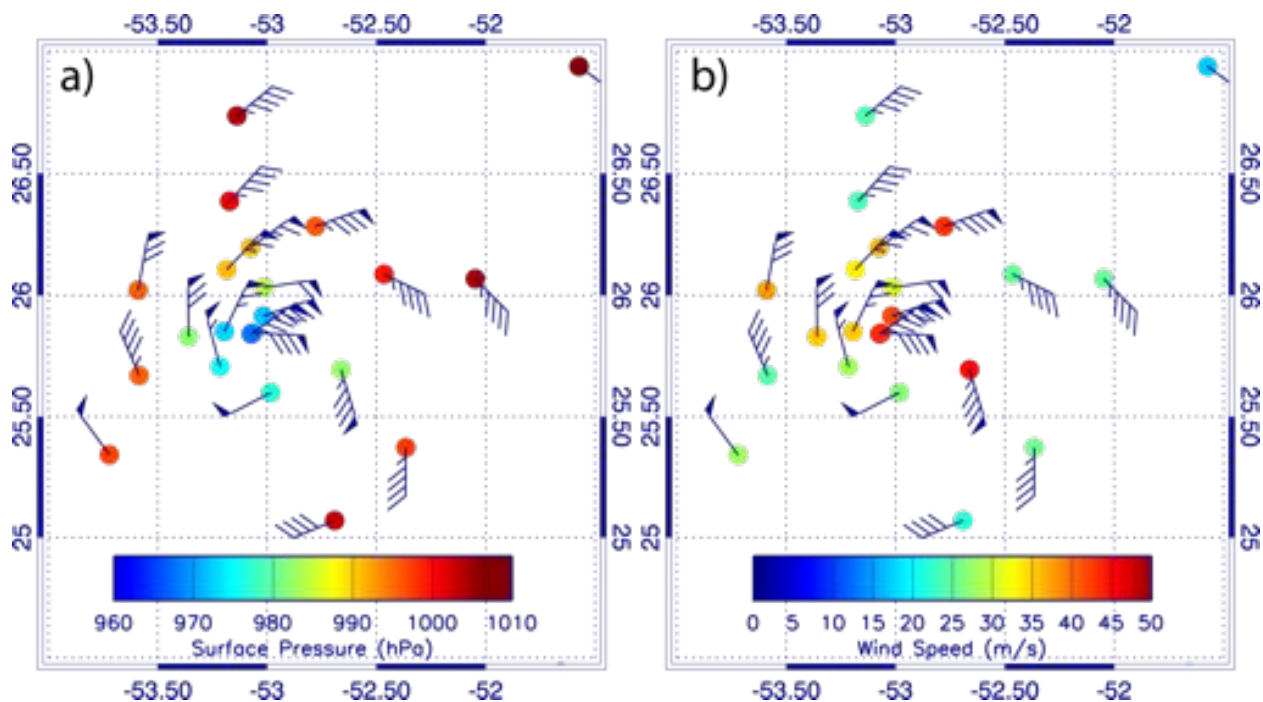
Figure 2. (a and b) Dropsonde-derived 800 hPa and 400 hPa relative humidity and (c) 200 hPa ground-relative wind speed (colored circles) from the 11-12 September 2014 flight. Color bars for relative humidity and wind speed are shown along the bottom of the figure. Wind barbs (full barb,  $5 \text{ m s}^{-1}$ ; half-barb,  $2.5 \text{ m s}^{-1}$ ; flags,  $25 \text{ m s}^{-1}$ ) show storm-relative winds at the respective altitudes. Dropsonde locations account for dropsonde drift and storm motion, with positions adjusted to a reference time of 0900 UTC 12 September. Data superimposed on GOES infrared imagery (IR) at 0845 UTC and SSMI/S 91 GHz polarization corrected temperature [color scale in (b)] at 0849 UTC 12 September. (d-f) Same as (a-c), but for a reference time of 0032 UTC 15 September and superimposed on GOES IR imagery at 0045 UTC 15 September. Satellite

623 imagery is from the Naval Research Laboratory Tropical Cyclone web page  
624 (<http://www.nrlmry.navy.mil/TC.html>).

625



626

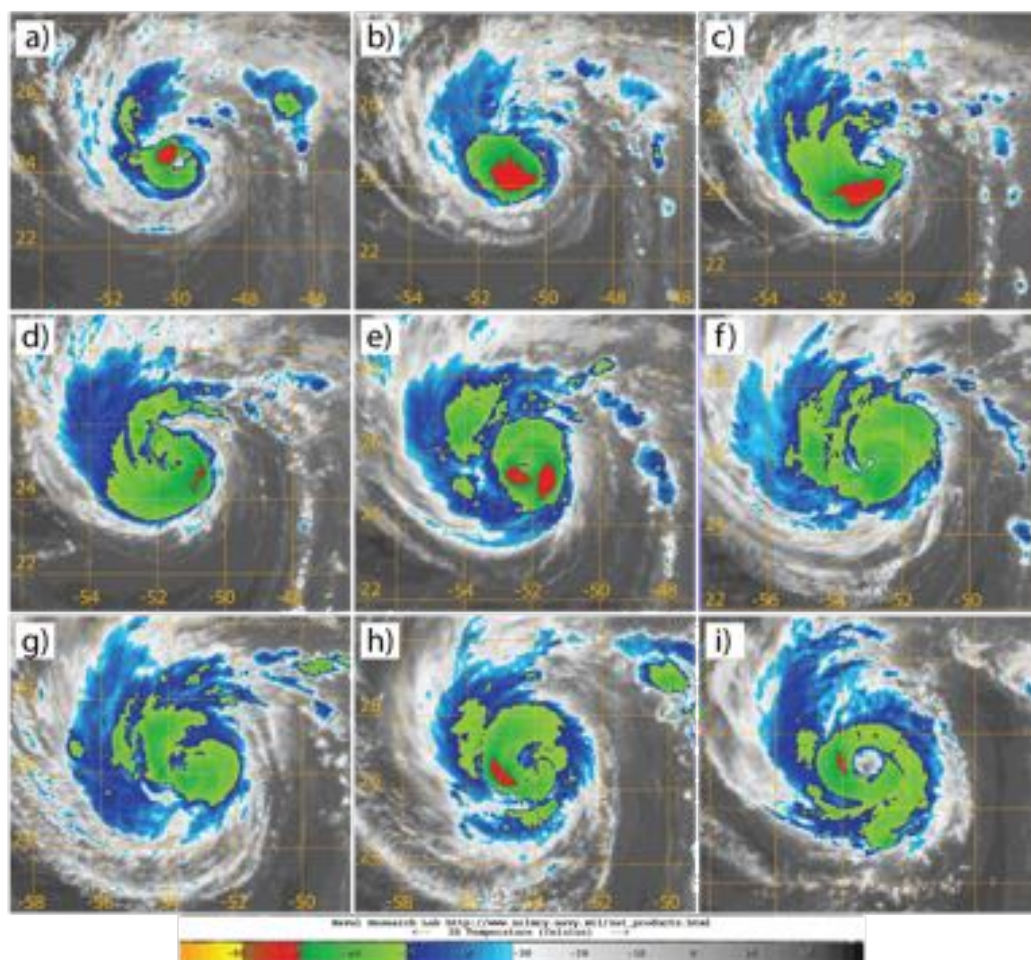


627

628 Figure 3. Plots of (a) surface pressure and (b) estimated 10-m ground-relative wind speed for the  
 629 14-15 September 2014 GH flight. Wind barbs (full barb,  $5 \text{ m s}^{-1}$ ; half-barb,  $2.5 \text{ m s}^{-1}$ ; flags,  $25 \text{ m s}^{-1}$ ) show storm-relative winds. Dropsonde positions are adjusted to a reference time of 0032  
 630  $\text{s}^{-1}$  UTC 15 September using the observed position and time of the near-surface observations and an  
 631 estimated storm motion based on the NHC-determined best track information.  
 632

633

634



635 Figure 4. GOES Infrared imagery (see color scale at bottom) from the Naval Research  
636 Laboratory tropical cyclone website for (a) 1115, (b) 1315, (c) 1515, (d) 1715, and (e) 2115 UTC  
637 14 September; and (f) 0045, (g) 0315, (h) 0715, and (i) 1315 UTC 15 September 2014.

638

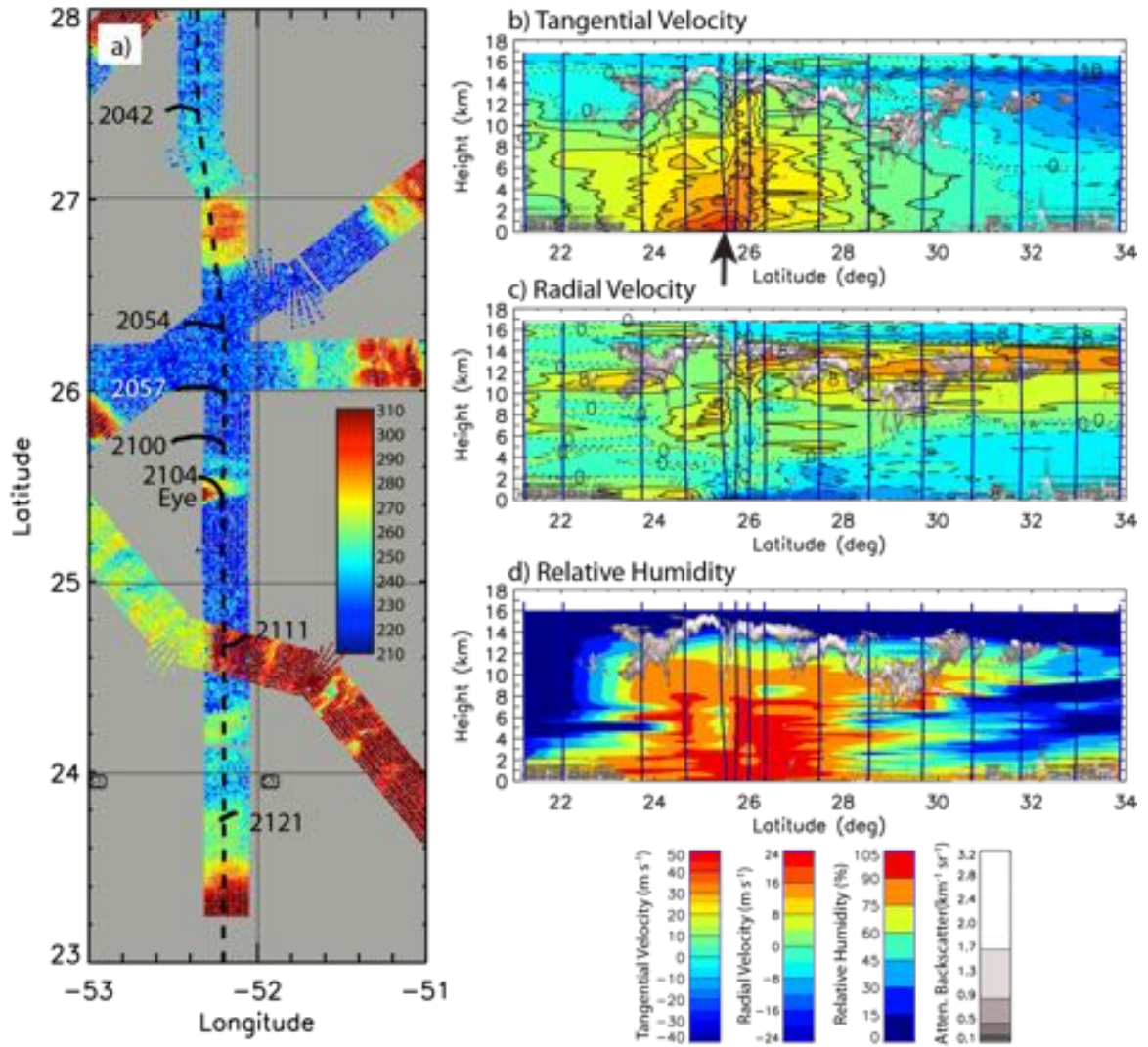


Figure 5. (a) S-HIS brightness temperatures (color shading, K) for the 895-900  $\text{cm}^{-1}$  channel. The eye of Edouard is labeled “Eye” near the warm brightness temperatures associated with the low clouds in the eye. The black dashed line shows the approximate flight path (line segments through dropsonde points only). Short curved line segments indicate dropsonde horizontal trajectories, with the release point coinciding with the flight path. Dropsonde times (UTC) are indicated. (b) Tangential velocity, (c) radial velocity, and (d) relative humidity with respect to water for temperatures  $\geq 273.15\text{K}$  and with respect to ice at colder temperatures (color shading) derived from dropsonde data between 1935-2207 UTC 14 September. Dropsonde locations are

648 indicated by vertical lines. Grey shading in right panels shows CPL attenuated backscatter (ABS,  
649  $\text{km}^{-1} \text{sr}^{-1}$ ) multiplied by 100. Vertical arrow in (b) indicates the location of the center dropsonde  
650 at 2104 UTC.

651

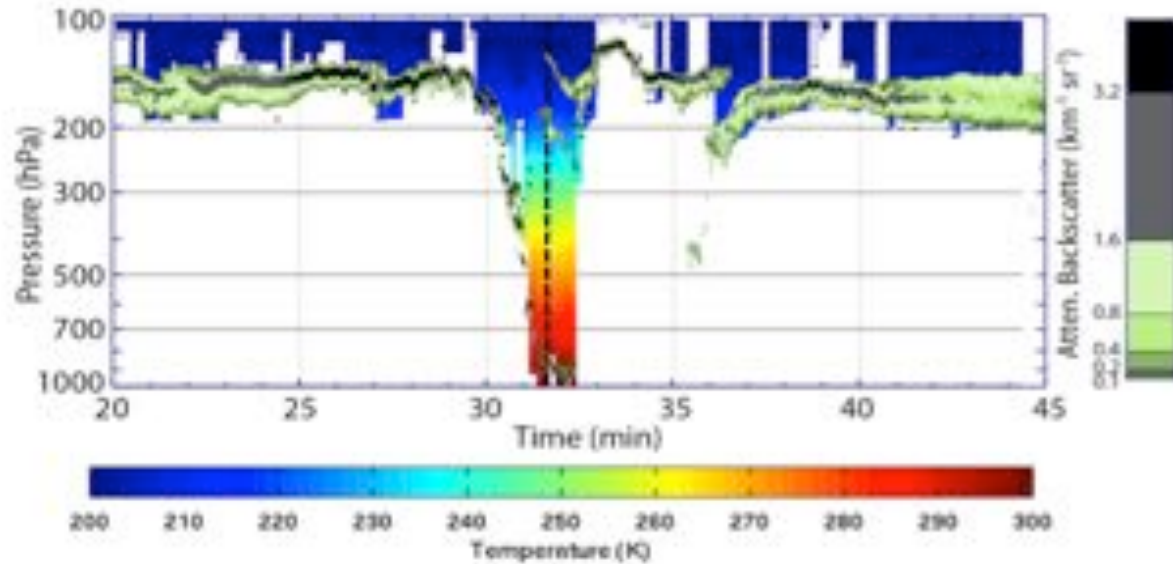


Figure 6. CPL attenuated backscatter ( $\times 100$ ) and S-HIS real-time retrieved air temperature for the period 0020-0045 UTC 15 September during a transit over the storm from northeast to southwest of the center. Vertical dashed line shows the location of the 0032 UTC 15 September dropsonde.

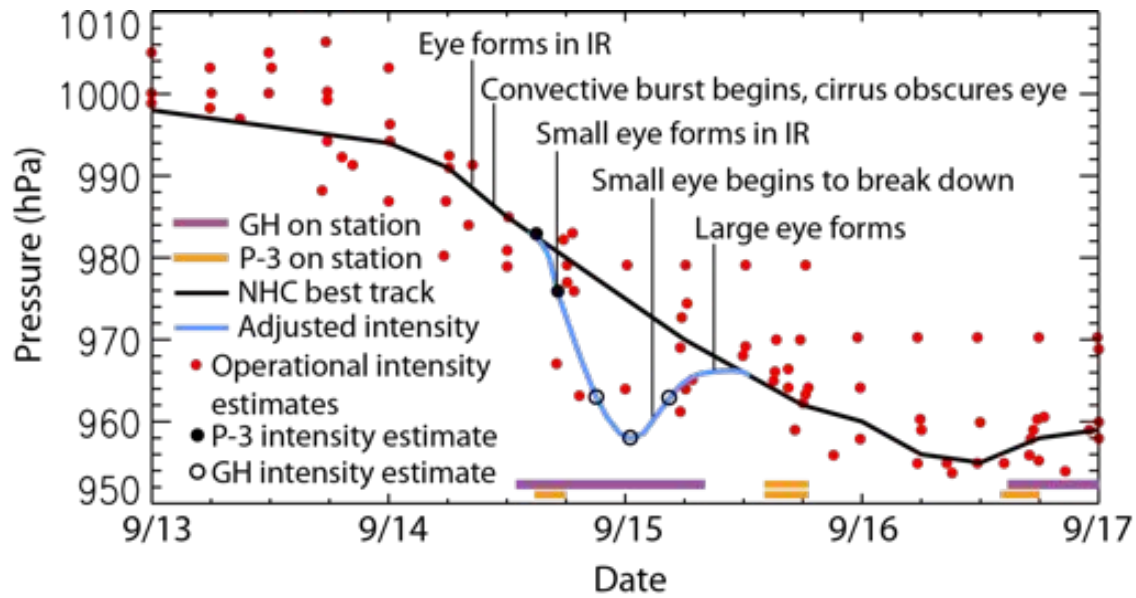


Figure 7. Time series of NHC best-track (black line) central pressure and operational intensity estimates (red circles, from satellite and aircraft). The blue line indicates estimated central pressures from P-3 (black circles) and GH (open circles) dropsondes. Orange and purple lines along the bottom of the figure indicate on-station times for NOAA P-3s and GH, respectively. Text indicates significant events during storm evolution.



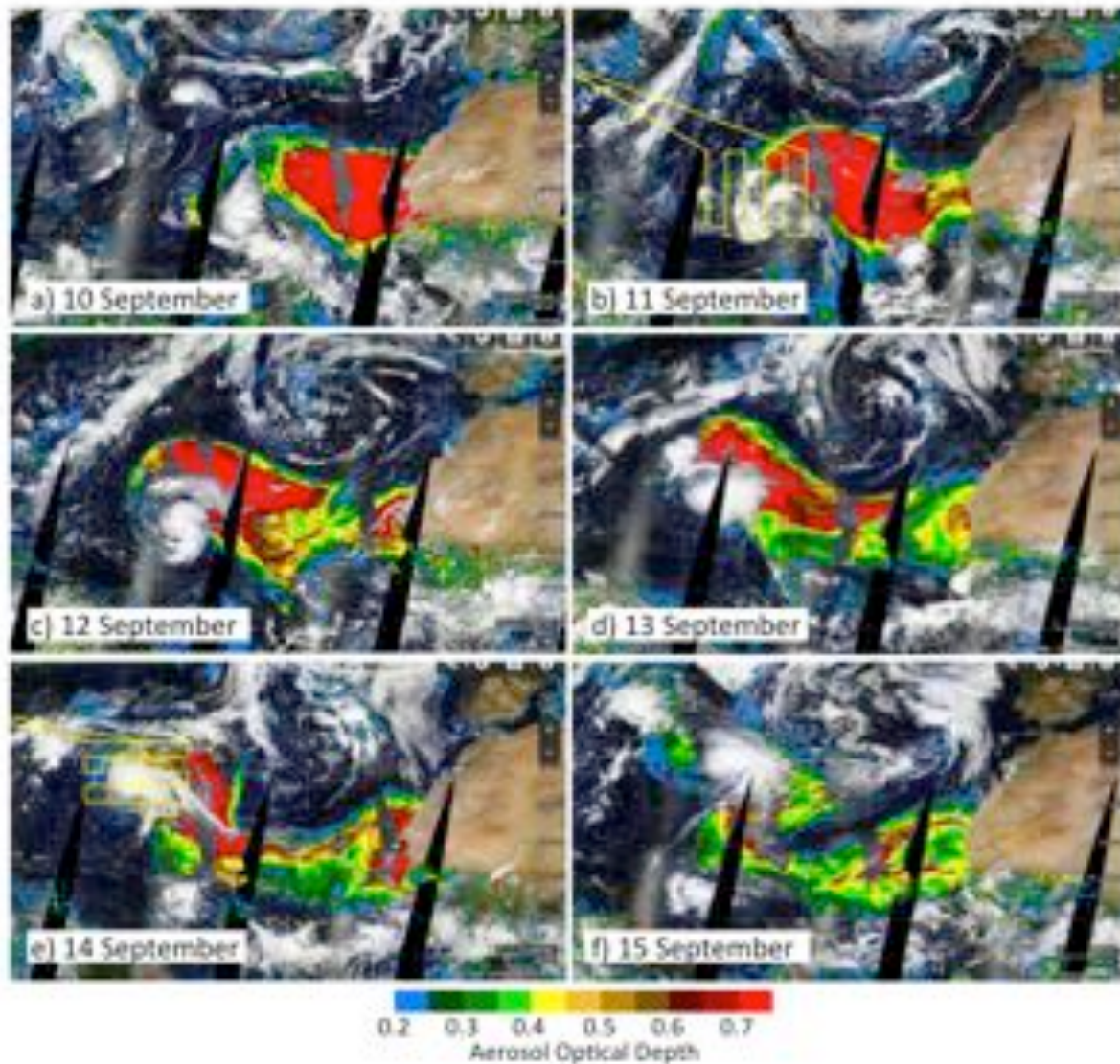
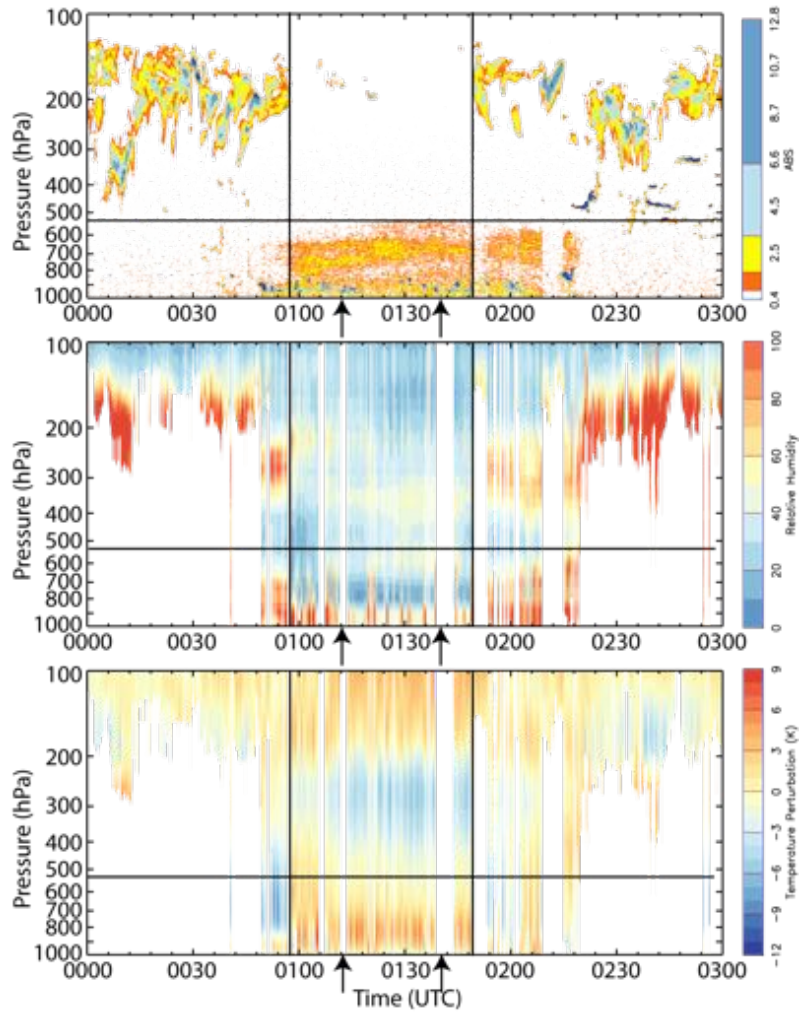


Figure 8. MODIS daily cloud and aerosol optical depth (colors) images show the evolution of the SAL outbreak near Hurricane Nadine on the indicated days. The flight track for the 11-12 September flight is shown in (b) and for the 14-15 September flight in (e). MODIS imagery obtained from the NASA Worldview web page (<https://earthdata.nasa.gov/labs/worldview/>).



671

672 Figure 9. (a) CPL aerosol backscatter ( $\times 100 \text{ km}^{-1} \text{ sr}^{-1}$ ) showing the dust layer north of Nadine  
 673 along the northern portions of the 5<sup>th</sup> and 6<sup>th</sup> north-south oriented flight legs (from left to right in  
 674 Fig. 8b) during the 11-12 September 2012 flight. S-HIS (b) relative humidity and (c) temperature  
 675 perturbation for the same flight segment. Temperature perturbations are derived by removing the  
 676 average temperature from 2000 UTC 11 September to 0600 UTC 12 September. The horizontal  
 677 line marks the top of the dust layer, and the vertical lines separate times of nearly clear skies  
 678 (0100-0149 UTC) from times with upper-level cloud cover. There is a reversal in the  
 679 temperature anomalies below 400 hPa and much higher low-level relative humidity before 0100



680 UTC and after 0149 UTC, suggesting possible retrieval biases caused by upper-level clouds.

681 Vertical arrows indicate the times of aircraft turns, first from northbound to eastbound, second

682 from eastbound to southbound.

683

684

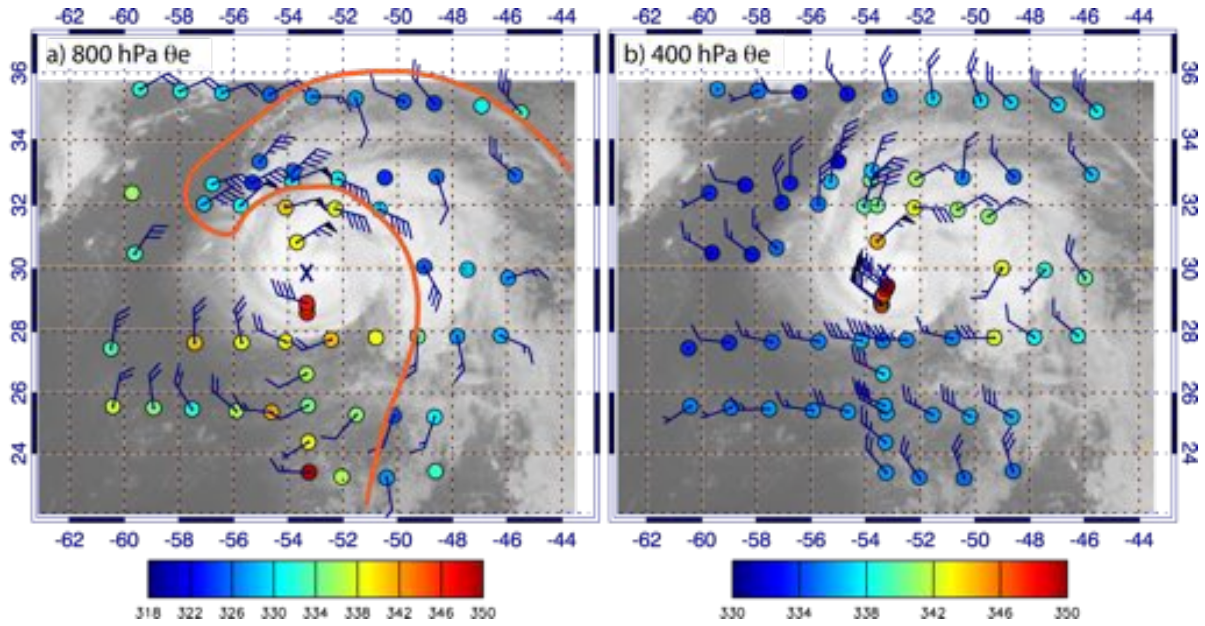


Figure 10. Equivalent potential temperature (colored circles) and storm-relative wind barbs (full barb,  $5 \text{ m s}^{-1}$ ; half-barb,  $2.5 \text{ m s}^{-1}$ ; flags,  $25 \text{ m s}^{-1}$ ) at (a) 800 hPa and (b) 400 hPa superimposed on the GOES infrared imagery at 0015 UTC 15 September 2012. Dropsonde locations account for dropsonde drift and storm motion, with positions adjusted to a reference time of 0000 UTC 15 September. Color bars indicate  $\theta_e$  values (K) corresponding to the dropsonde data in each panel.

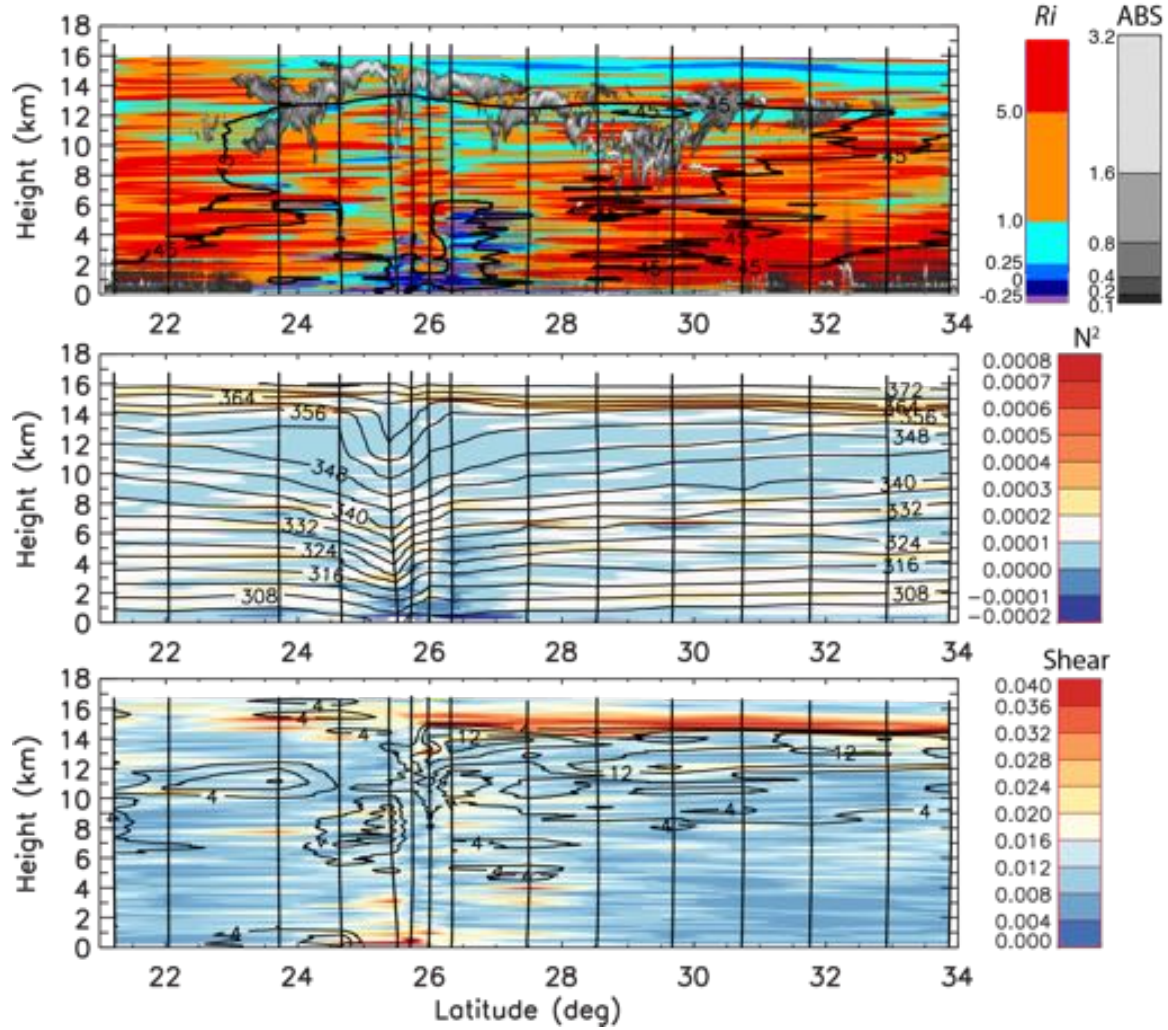


Figure 11. Plots of (a) bulk Richardson number and CPL attenuated backscatter ( $\times 100 \text{ km}^{-1} \text{ sr}^{-1}$ ), (b) Brünt-Vaisala frequency,  $N^2 \text{ (s}^{-2}\text{)}$ , and (c) vertical wind shear,  $S \text{ (s}^{-1}\text{)}$ , for the Edouard cross section shown in Fig. 5. In (a), the 45% relative humidity contour is shown to indicate an approximate boundary of very dry air. In (b), contours are of potential temperature at 4 K intervals while in (c) contours show outflow regions with radial velocity at  $4 \text{ m s}^{-1}$  intervals starting at  $4 \text{ m s}^{-1}$ .

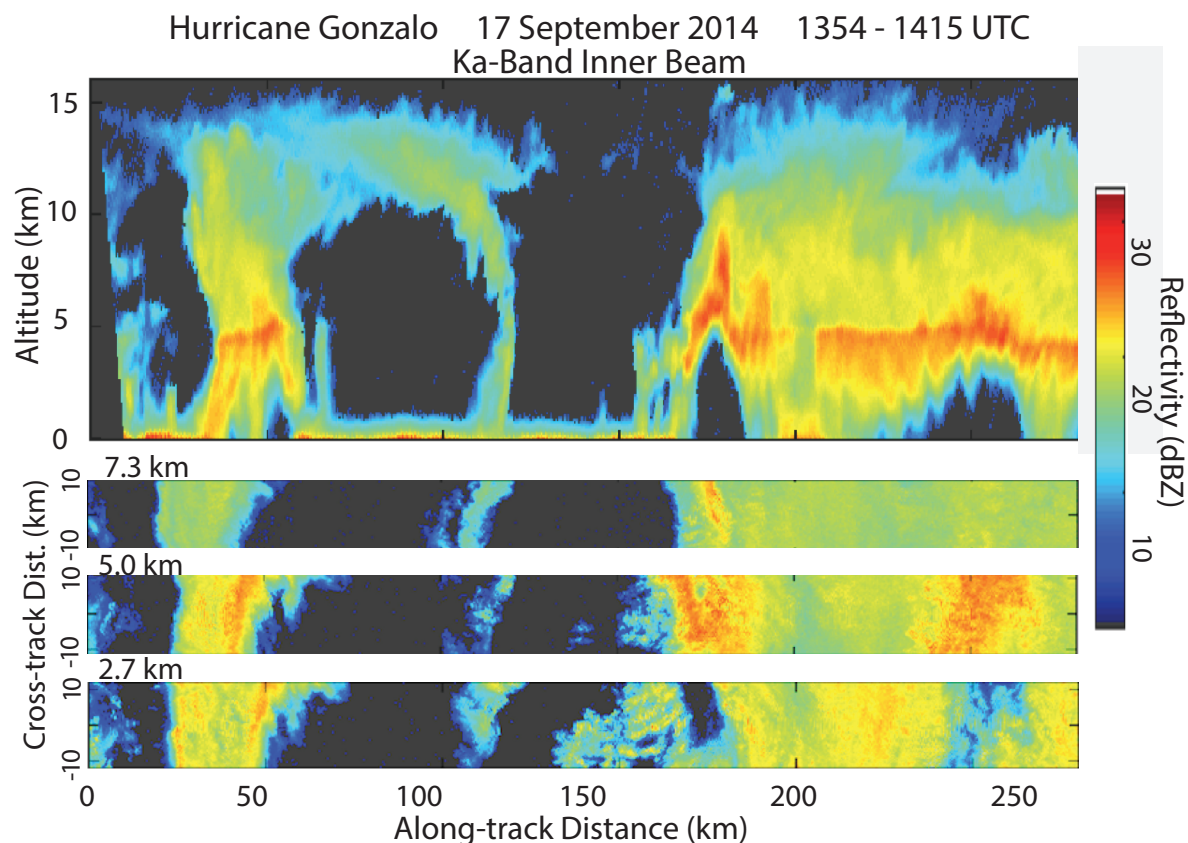


Figure S1. Hurricane Gonzalo on 17 September 2014 as observed from the HIWRAP Ka-band frequency as the storm was approaching Bermuda. Vertical cross section (top) and horizontal cross sections at 2.7, 5.0 and 7.3 km altitude (bottom panels) reconstructed from HIWRAP conical scanning outer beam. Both inner and outer eyewalls are observed at 110 and 160 km, and 40 and 250 km, respectively. The Ka-band data shown has higher resolution than the Ku-band and is more sensitive to light precipitation at upper levels in the eyewall, but suffers more attenuation in heavy rain near the surface.